



# Influence of Multiaxial Cryoforging on Microstructural, Mechanical, and Corrosion Properties of Copper-Titanium Alloy

S. Ramesh , H. Shivananda Nayaka, Sandeep Sahu, K.R. Gopi, M.J. Shivaram, and Shashibhushan Arya

(Submitted July 2, 2019; in revised form October 22, 2019; published online November 18, 2019)

Multiaxial forging (MAF) was used to process Cu-4.5%Ti (wt.%) alloy at cryogenic temperature up to three cycles with a cumulative strain of 1.64. Microstructures, mechanical, and corrosion properties of as-received and deformed samples were analyzed. Microstructural analysis showed that average grain size decreased from 70  $\mu\text{m}$  to 200 nm, and electron backscattered diffraction (EBSD) analysis revealed the transformation of high-angle grain boundaries (HAGBs) to low-angle grain boundaries (LAGBs). Variations in intensity of peaks were observed by x-ray diffraction (XRD) technique. Microstructural investigation showed elongated grains with shear bands having width  $\sim 200$  nm for 3-cycle sample. Tensile testing and micro-hardness tests showed improvements in ultimate tensile strength (UTS), yield strength (YS), and micro-hardness, with the increase in MAF cycles. Ultimate tensile strength and hardness increased from 605 MPa and 252 HV (for as-received) to 1284 MPa and 428 HV for three cycles of MAF-processed sample, respectively. Improvement in strength and hardness was attributed to refined grain structure. Corrosion study was carried out for different cycles of MAF-processed samples using potentiodynamic polarization, and corroded surfaces were analyzed using scanning electron microscopy (SEM) and energy-dispersive spectroscopy (EDS) analysis.

**Keywords** corrosion resistance, Cu-Ti alloy, fractography, mechanical properties, multiaxial cryoforging

## 1. Introduction

Automobile and aerospace industries widely use materials having ultrafine grain structures that are commonly obtained using severe plastic deformation (SPD) techniques (Ref 1-5), as they possess superior mechanical properties like high strength, fatigue, ductility, and fracture resistance. Some of the SPD techniques developed in the past few decades are equal-channel angular pressing (ECAP) (Ref 6-8), accumulative roll bonding (ARB) (Ref 9-11), multiaxial forging (MAF) (Ref 12-14), repetitive corrugation and straightening (RCS) (Ref 15, 16), high-pressure torsion (HPT) (Ref 17, 18), twist channel angular pressing (TCAP) (Ref 19), twist channel multiangular pressing (TCMAP) (Ref 20), and machining (Ref 21, 22). Samples processed by MAF have ultrafine grains/nanocrystalline structure. It does not require any special tools and equipments. It is a simple repeated compression process with a rotation of  $90^\circ$

during each pass to apply load, and large plastic strains are imposed in the sample.

Magnesium alloy Mg-Al-Zn was processed at room temperature using MAF at  $\epsilon = 2$  by Miura et al. (Ref 23). After 20 MAF passes, strength increased to 525 MPa. Joshi et al. (Ref 24) processed Al-2014 alloy by MAF under cryogenic condition for four cycles with  $\epsilon = 2.4$ . It was found that the ultrafine grains were formed in the range of 100-450 nm due to which hardness increased from 103 to 171 HV and fracture toughness increased from 23.93 to 37.7  $\text{MPa}\cdot\text{m}^{0.5}$ . Yang et al. (Ref 25) processed AZ31 magnesium alloy by MAF under decreasing temperature condition for every pass. Low-temperature MAF was found to accelerate the development of fine grain structure and plastic workability. Padap et al. (Ref 26) processed plain low-carbon steel at 500  $^\circ\text{C}$  using MAF. After nine passes of MAF, strength and hardness increased from 357 to 791 MPa and from 120 to 252 HV, respectively. As MAF passes increased, low-angle grain boundaries (LAGBs) transformed to high-angle grain boundaries (HAGBs) and grain size reduced to 0.5  $\mu\text{m}$ . Dasharath et al. (Ref 27) used MAF to process Cu-9.6 Zn% at cryogenic temperature at  $\epsilon = 3, 5.4,$  and 7.2. It was found that there was an increase in YS from 70 to 680 MPa, and hence, it was observed that dimple size and shear fracture angle decreased during fractured surface analysis. Wei et al. (Ref 28) investigated the corrosion behavior of Cu-Ti alloys with varying Ti contents in 3.5% NaCl solution. Cu matrix (Ti dissolved) changed the corrosion behavior compared to pure Cu that showed active-passive and trans-passive corrosion. Wei et al. (Ref 29) processed Cu-4% Ti alloy by different aging conditions and investigated the corrosion behavior. Both pitting and intergranular corrosion were observed over the surface of sample. Traces of Cu phases and precipitates of  $\beta\text{-Cu}_4\text{Ti}$  were found in the refined microstructure in alternate layers, which improved the corrosion resistance,

S. Ramesh and H. Shivananda Nayaka, Severe Plastic Deformation Laboratory, Department of Mechanical Engineering, National Institute of Technology Karnataka, Surathkal 575025, India; Sandeep Sahu, Department of Materials Science and Engineering, Indian Institute of Technology Kanpur, Kanpur 208016, India; and K. R. Gopi, Department of Mechanical Engineering, Malnad College of Engineering, Hassan 573201, India; M.J. Shivaram and Shashibhushan Arya, Department of Metallurgical and Materials Engineering, National Institute of Technology Karnataka, Surathkal 575025, India. Contact e-mail: ramnitk2016@gmail.com.

and enveloping effect was developed. Wang et al. (Ref 30) investigated the potentiodynamic polarization effect and electrochemical impedance spectroscopy (EIS) of copper using 3.5% NaCl and observed the inhibition of domperidone on copper. It was concluded that domperidone played the role of anodic inhibitor with 94.2% efficiency. Scanning electron microscopy (SEM) and atomic force microscopy (AFM) images showed copper corrosion that was inhibited due to absorption.

Copper beryllium (Cu-Be) has been found to show the highest strength level among copper alloys. Moreover, these alloys demonstrate good formability and electrical conductivity during both hot working and cold working (Ref 28). The main drawback of Cu-Be alloy is its high price and toxic nature. Copper-titanium (Cu-Ti) alloy is the nontoxic substitute for Cu-Be, and it shows good mechanical and electrical properties and can be used for the production of high-strength spring, corrosion-resistant elements, and electrical connections like contact, relay, gears, and electrical wires (Ref 31, 32). More study is necessary to increase the usage of Cu-Ti alloy in engineering applications with increased mechanical properties.

From the aforementioned literature, it can be observed that MAF processing can be used for improving the mechanical properties and microstructural modification. However, there has been a limited research in improving the strength and ductility of Cu-Ti alloy. MAF at cryogenic temperature can produce more refined microstructure, as recovery and recrystallization are completely suppressed at cryogenic temperature, resulting in high dislocation densities and other defects, especially in materials having low stacking fault energy.

In this context, the present work investigates the applicability of MAF process on Cu-4.5%Ti alloys for improving microstructural features and mechanical properties involving uniaxial tensile test and Vickers micro-hardness test. Microstructural evolution was studied using electron backscattered diffraction (EBSD), SEM, transmission electron microscopy (TEM), and x-ray diffraction (XRD) analysis.

## 2. Materials and Experimental Procedure

Cu-4.5%Ti, having chemical composition (wt.%) of 4.5 Ti, 0.13 Zn, 0.03 Mn, 0.07 P, 0.01 Ni, and remaining copper were used in this study. Hot die steel was used to fabricate MAF die. Die design was based on plane strain condition. After die fabrication, the die was heat-treated to maintain the hardness of 52 HRC. MAF and its notations are schematically shown in Fig. 1(a) and (b). Cu-4.5%Ti was obtained in the form of rectangular blocks of dimensions  $30 \times 30 \times 25 \text{ mm}^3$ . Homogenization of these blocks was done at  $850 \text{ }^\circ\text{C}$  for 24 h. Resulting samples were called as 'as-received' sample. MAF was carried out on a hydraulic press of 200 Ton capacity, with 0.03 mm/s strain rate. Dimension ratio of 1.2:1.2:1 was maintained throughout MAF processing. For achieving stable temperature, samples were immersed in liquid nitrogen for 20 min before processing by MAF. Forged sample was once again immersed in liquid nitrogen for 5 min and pressed by rotating the sample by  $90^\circ$ . Further forging was carried by rotating the sample at  $90^\circ$  in the third direction, thus completing one cycle of MAF, as shown in Fig. 1(b). MAF was carried out up to three cycles. During each forging pass, a strain of 0.182 was induced into the material, according to the equation,

$$\varepsilon = \ln\left(\frac{h_0}{h}\right)$$

where  $h_0$  and  $h$  are the initial and final heights of the sample, respectively.

For microstructural characterization and mechanical testing, sample was cut from the middle region in a plane perpendicular to the forging axis of the final pass of the MAF cycle, as shown schematically in Fig. 2(a). ASTM E8 M standard was used to prepare the tensile sample of gauge length of 16 mm and diameter of 4 mm. Tensile test was performed on Shimadzu AG-X plus<sup>TM</sup> 100 kN tensile tester at room temperature with a strain rate of 0.5 mm/min. Omni-Tech micro-hardness tester was used to estimate micro-hardness of the MAF-processed samples with 100 g load and 15-s dwell period. Indentations were made at 15 different locations as shown in Fig. 2(b), and average values are reported here. Samples were polished on emery papers sequentially up to 2000 grade, followed by cloth polishing using alumina powder of size 1 and  $0.05 \text{ }\mu\text{m}$  diamond paste. Polished samples were etched using 10 g potassium dichromate ( $\text{K}_2\text{Cr}_2\text{O}_7$ ), 5 mL  $\text{H}_2\text{SO}_4$ , 2 mL HCl, and 95 mL distilled water for around 5 sec and thoroughly cleaned using water to remove the traces of acid. Microstructures were observed using optical microscopy (OM) (Zeiss AX10 LAB A1), SEM (JEOL JSM-6380LA), and TEM (JOEL JEM-2100). Samples were electropolished using the electrolyte containing 20% phosphoric acid ( $\text{H}_3\text{PO}_4$ ), 50% distilled water, 25% ethanol, 5% propanol at 10 V and 15 s at  $-15 \text{ }^\circ\text{C}$ , for EBSD analysis, which was performed on field emission scanning electron microscope (FESEM) (JEOL JSM-7100F) attached with Oxford Instruments' Nordlys detector. EBSD scanning area was  $465 \times 347 \text{ mm}^2$ , and camera binning mode was kept at  $4 \times 4$ . Voltage of 20 KeV with the step size of  $1 \text{ }\mu\text{m}$  was used to operate the EBSD, and Kikuchi patterns were indexed for Cu phase. HKL Channel 5 Tango software was used for post-processing orientation image microscopy (OIM) characterization.

An electrochemical corrosion study was conducted on as-received and MAF-processed samples. Samples used for this study was mirror-finished using polishing cloth and alumina solution. EC Lab-Bio Logic SP-150 electrochemical workstation, with three standard electrodes, was used. Saturated calomel and platinum wire were used as reference and counter electrodes, respectively. Sample of  $1 \text{ cm}^2$  was exposed to 3.5 wt.% NaCl electrolyte, which acts as a working electrode. Frequency from 100 kHz to 10 MHz was selected for potentiodynamic polarization with a scanning rate of 1 mV/s. Samples were immersed for 90 min in the electrolyte solution for stabilizing the open-circuit potential (OCP) before starting potentiodynamic polarization test.

## 3. Results and Discussion

### 3.1 Microstructural Analysis

Figure 3(a) shows the optical micrograph of as-received sample, having equiaxed grains with grain size of  $70 \text{ }\mu\text{m}$  with small fraction of twins. The microstructure consists of  $\alpha$ -Cu as matrix, and  $\beta$ - $\text{Cu}_4\text{Ti}_3$  is the secondary phase as marked in Fig. 3(a). Figure 3(b) shows the microstructure of one cycle of

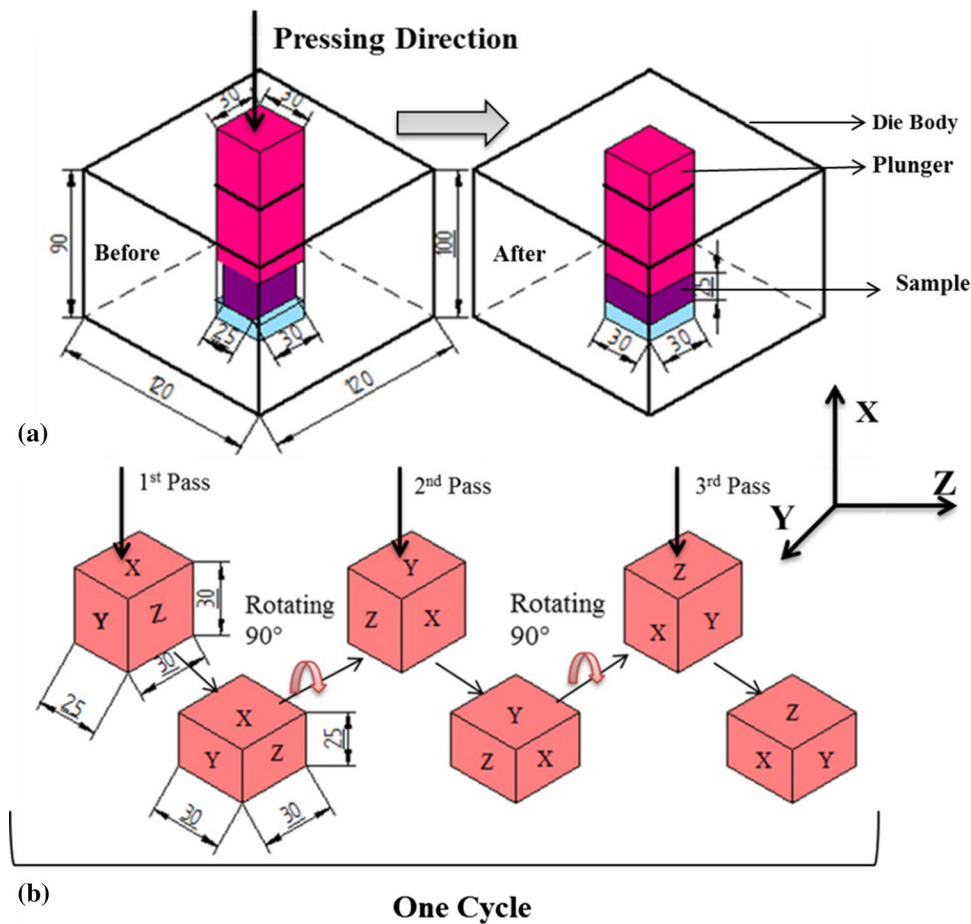


**Fig. 1** Schematic of (a) MAF process and (b) MAF notation for one cycle

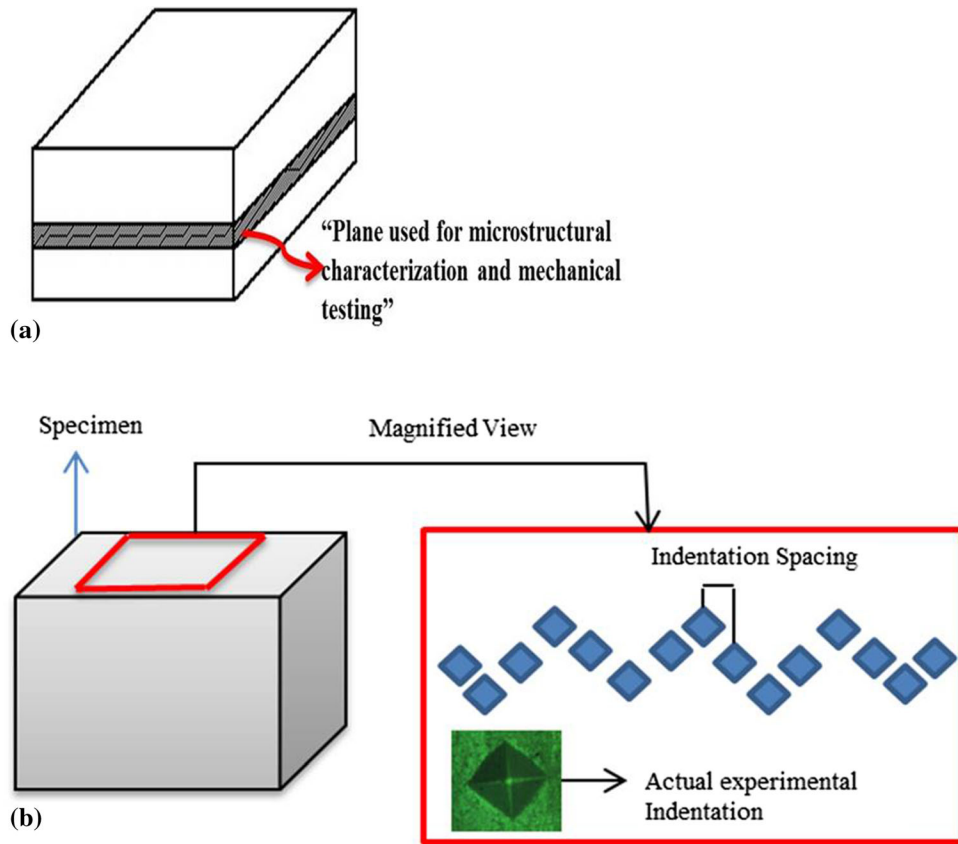
MAF-processed sample, with the formation of shear bands within the grains and grain size of  $5\ \mu\text{m}$ , and  $\beta\text{-Cu}_4\text{Ti}_3$  secondary phases are seen along the grain boundaries. Figure 3(c) shows the optical micrograph of two cycles of MAF-processed samples ( $\epsilon = 1.09$ ), indicating the formation of shear bands. Grain boundary become ambiguous and identification of individual grains became difficult, because of high-density shear bands, which directly depends on the accumulated strain at higher forging cycles. After two cycles of MAF, secondary phase distribution was more uniform as compared to one cycle of MAF-processed samples as marked in Fig. 3(c). Figure 3(d) shows the optical micrograph of three cycles of MAF-processed sample, with cumulative strain of 1.64. Fine subgrain and high-density shear bands were observed, with a reduction in gap between the shear bands. Similar micrographs were observed in multi-axial cryoforged copper (Ref 32) and Al 6061 alloys (Ref 15). At low temperature, shear bands are easily developed under SPD conditions. Finally, elongated type of grain substructure was observed (Ref 27). Figure 4 shows the SEM micrographs of as-received and MAF-processed samples. Figure 4(b) shows the microstructure of one cycle of MAF-processed Cu alloy, which shows the formation of shear bands formed within the grain. Figure 4(c)-(d) shows the increasing density of shear bands, and it is difficult to identify the individual grains after three cycles of MAF.

Figure 5 depicts the TEM micrographs of samples processed by two and three cycles of MAF, with insets showing

electron diffraction patterns. Figure 5(a) and (b) shows the formation of shear bands of  $800\ \text{nm}$  thickness in samples deformed by two cycles of MAF processing. Figure 5(c) shows that the electron diffraction pattern of two cycles of sample indexed and zone axis (Z) was  $[011]$ , as marked on the same pattern. Figure 5(d)-(e) shows the TEM micrograph of three cycles of cryoforged sample and 5(f) shows an electron diffraction pattern of the same sample. Three cycles of electron diffraction pattern contain continuous rings, and indexed planes are (101), (110), (111), (200), and (113). After three cycles, shear band thickness reduced to  $200\ \text{nm}$  with an increase in shear band density because of the accumulation of large strain. Figure 5(b) and corresponding electron diffraction pattern (Fig. 5c) show periodically arranged spotted rings with broad and bright regions that are stretched because of diffraction from elongated grains. Electron diffraction pattern in Fig. 5(f) shows continuous and narrow rings, which might be because of fine grains with LAGBs.

### 3.2 EBSD and Texture Analysis

Figure 6(a)-(d) shows that OIM analyzed the inverse pole figure (IPF) maps of as-received and MAF-processed samples. Crystallographic orientations were observed and are expressed by corresponding colors in standard stereographic triangle (Fig. 6e). As-received sample shows coarse equiaxed grains (with average grain size  $\sim 70\ \mu\text{m}$ ) that change to fine



**Fig. 2** (a) Schematic of section used for microstructure and mechanical testing and (b) schematic diagram of micro-hardness testing

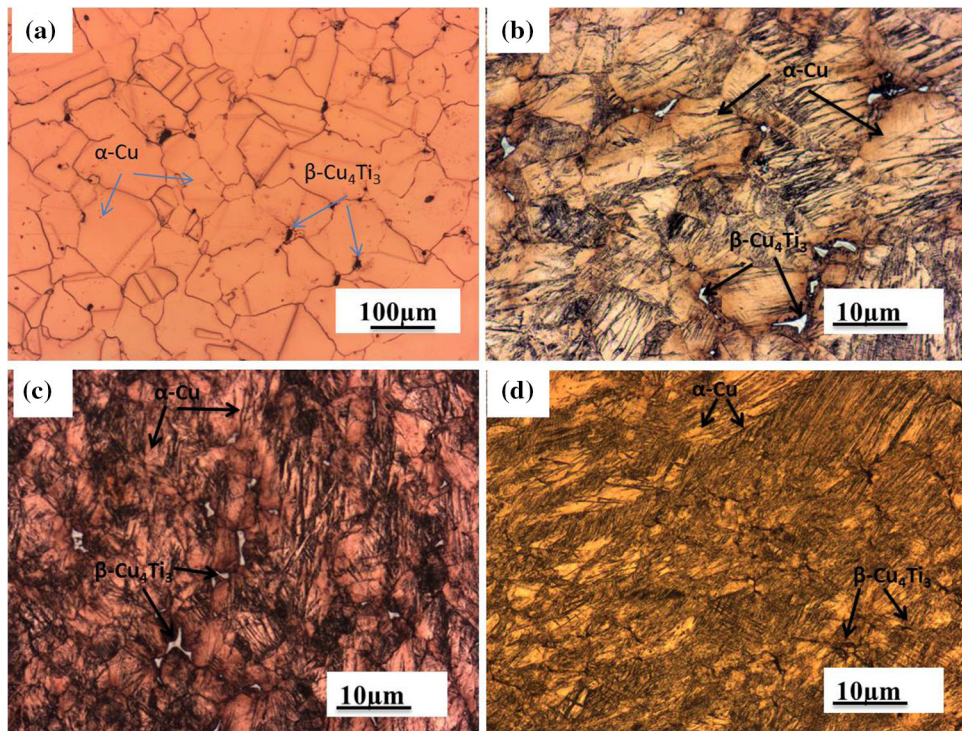


**Fig. 3** Optical micrographs of sample processed by different MAF cycles: (a) as-received, (b) one cycle, (c) two cycles, (d) three cycles

elongated grains (having grain size  $\sim 200$  nm) after three cycles of MAF processing. Misorientation angle distribution of as-received and MAF-processed samples is shown in Fig. 7.

After one cycle, the fraction of low-angle misorientation ( $2^\circ$ - $15^\circ$ ) is low as compared to other conditions. Strong peak was observed at high angle ( $60^\circ$ ) and at low angle ( $2^\circ$ ), which may

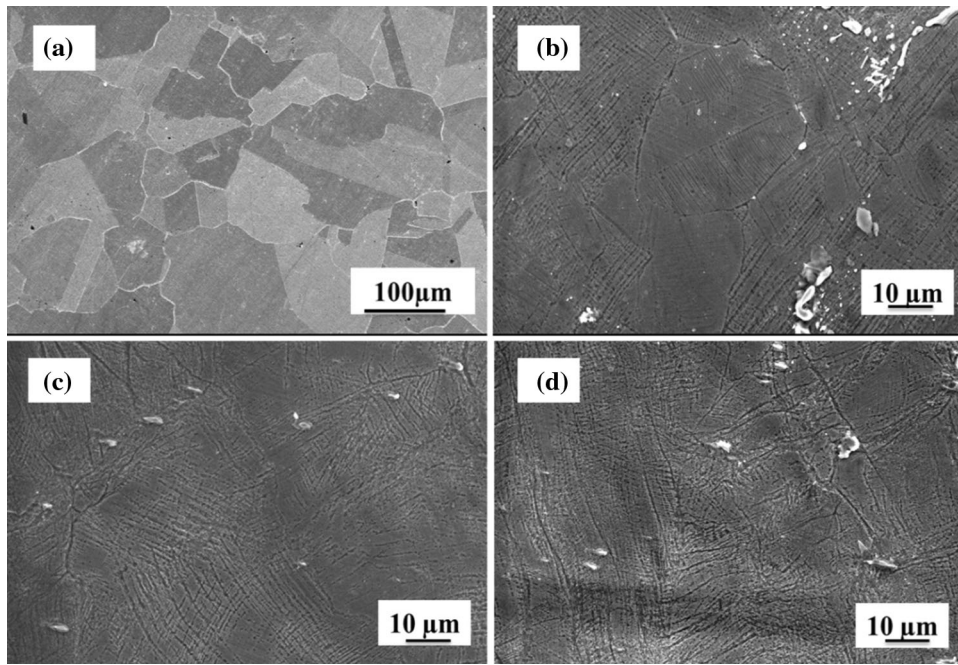


**Fig. 4** SEM images of sample processed by different MAF cycles: (a) as-received, (b) one cycle, (c) two cycles, (d) three cycles

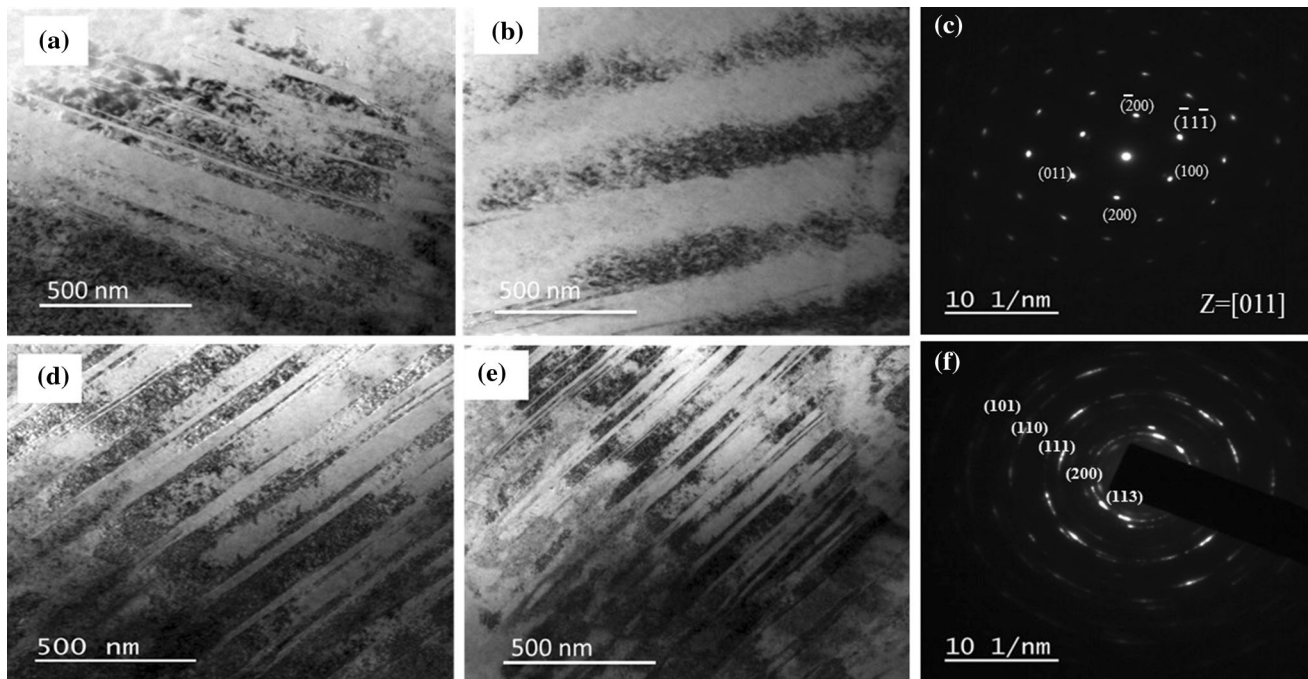


**Fig. 5** TEM micrographs of MAF-processed (a-b) two cycles, (c) electron diffraction pattern of two cycles and (d-e) three cycles of samples, (f) electron diffraction pattern of three cycles

be due to grain refinement mechanism. At higher cycles of MAF, strain accumulated in sample increases and HAGBs get converted to LAGBs (Ref 33-35), leading to more stable microstructure. Grains elongated and oriented in one direction were found in samples processed at three MAF cycles. Initial texture ranged from (100) to (111) having coarser grains, as visible from IPF map (Fig. 6). After MAF processing, coarse grains are refined and converted from HAGBs to LAGBs, as

shown in Fig. 7(b-d). Texture (111) starts increasing after one cycle (indicated by blue color in Fig. 6b-d).

### 3.3 XRD Analysis

XRD peaks are shown in Fig. 8. Cu,  $\text{Cu}_4\text{Ti}_3$ , and  $\text{Cu}_3\text{Ti}_2$  phases are observed from XRD peaks. Change in intensity and broadening of peaks of planes (111), (220), (200), and (311) are observed in samples processed by MAF up to two and three

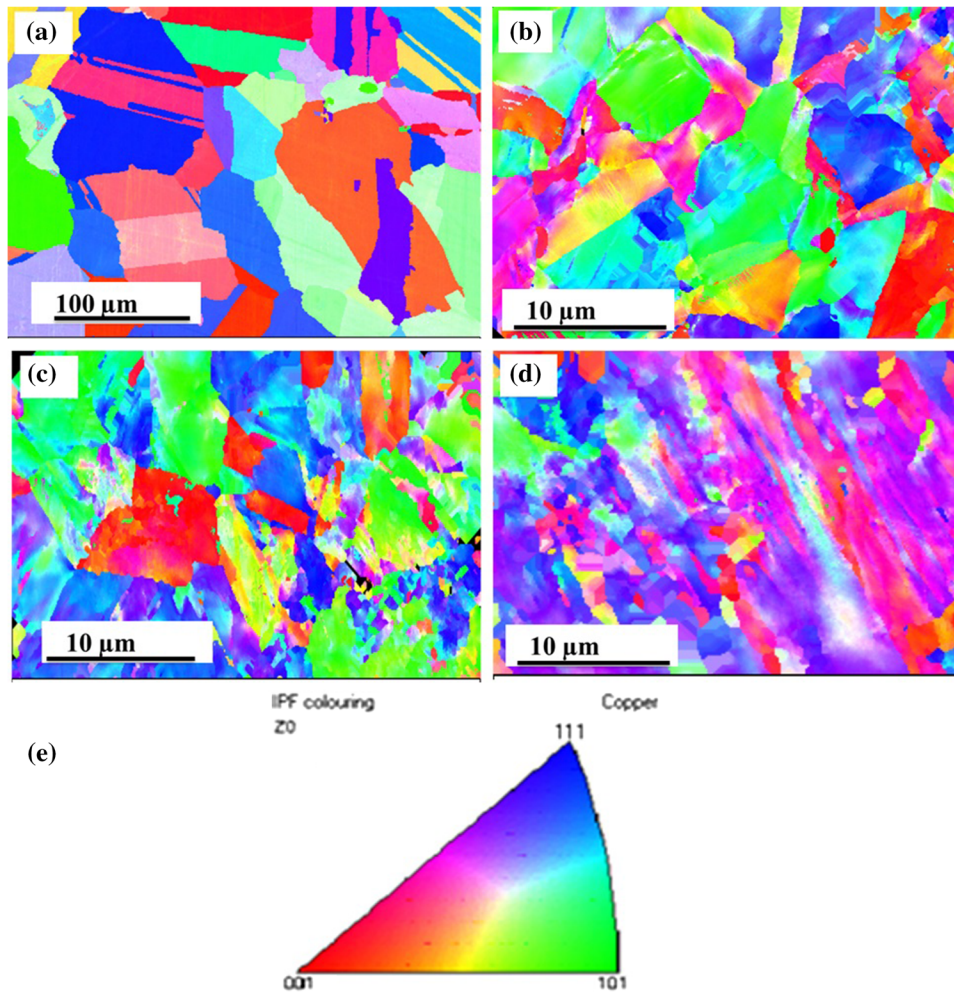


**Fig. 6** OIM analyzed IPF map of (a) as-received, (b) MAF one cycle, (c) MAF two cycles, (d) MAF three cycles, and (e) standard stereographic triangle for inverse pole figure

cycles. Observed changes are because of grain refinement and strain hardening during MAF processing and the induced lattice strain (Ref 36). Change in texture was observed when the material was processed by MAF and is evident from Fig. 8. Further, strong variations in the intensities of the peaks are observed, and also peaks are shifted by one degree after three cycles of MAF, which might be because of high strain in the sample.

### 3.4 Mechanical Properties

Engineering stress–strain curve is shown in Fig. 9(a), and corresponding mechanical properties are depicted in Fig. 9(b) and Table 1. From Fig. 9(b), it was noticed that YS and UTS increased as the number of forging cycles increased. UTS, YS, and elongation for as-received samples were measured and found to be 641 MPa, 442 MPa, and 16%, respectively. After one MAF cycle ( $\epsilon = 0.54$ ) at cryogenic temperature, UTS and

YS increased, respectively, to 861 and 759 MPa, but percent elongation reduced to 10%. After two cycles of MAF, UTS increased to 1016 MPa, YS improved to 926 MPa, and elongation raised to 11%, due to decrease in twin space width and decrease in shear band width. Maximum tensile strength was obtained for three cycles (1284 MPa), and percentage elongation came to 12%. The increase in strength is due to grain refinement. In addition, the decrease in twin width plays a major role in the improvement of strength and ductility, during MAF (Ref 37). The relationship between strength (YS and UTS), hardness, and average grain size is represented in Fig. 10(a). This figure clearly shows the improvement in strength and hardness with the decrease in grain size. Figure 10(b) shows that the relation between yield strength and the inverse square root of grain size, and can easily be related to the well-known Hall–Petch equation (Ref 38). A similar kind of behavior between strength and grain size was also obtained by

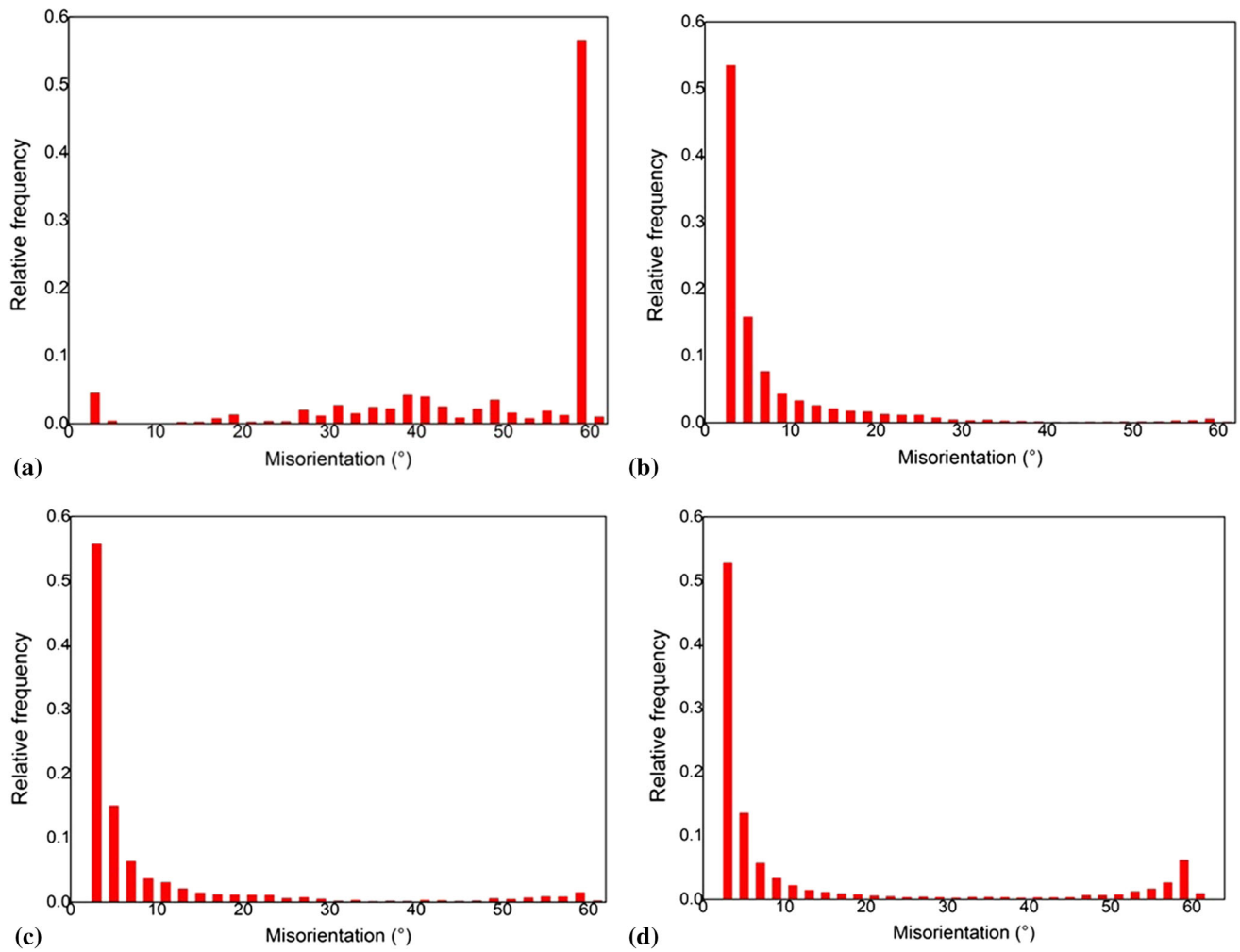


**Fig. 7** Misorientation angle distribution of samples processed by different MAF cycles: (a) as-received, (b) one cycle, (c) two cycles, and (d) three cycles

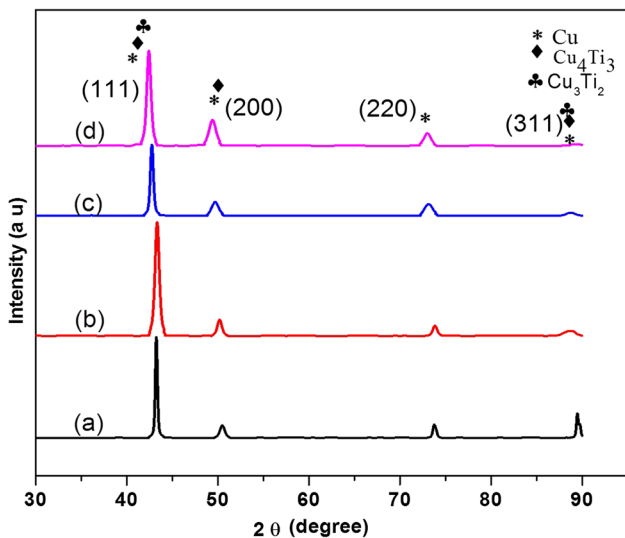


**Fig. 8** XRD of samples processed by different MAF cycles: (a) as-received, (b) one cycle, (c) two cycles, and (d) three cycles

Luo et al. (Ref 39-41). Theoretically, the Hall-Petch equation was determined from the graph with the help of slope.  $\sigma_{Yield} = 440 + (1.63 \cdot d^{-1/2})$ ; this is the Hall-Petch equation obtained from the graph.

Omni-Tech hardness machine was used to find Vickers micro-hardness (HV) of undeformed and deformed samples. Hardness of as-received material was 252 HV. After the first cycle of MAF, hardness increased to 358 HV. Hardness increased to 392 and 428 HV, respectively, in the samples processed up to two and three cycles of MAF and is shown in Fig. 11. Grain refinement and strain hardening are the reasons for the increase in hardness of the sample.

### 3.5 Fractography

Fracture surface was analyzed using SEM. Figure 12(a) shows the fracture surface of as-received sample, and it contains large-sized dimples of  $\sim 25 \mu\text{m}$  over the entire surface, and it is a ductile type fracture. Figure 12(b) shows one cycle of MAF-processed sample's fracture surface where the dimple size decreased to  $6 \mu\text{m}$ . From Fig. 12(c) and (d), it

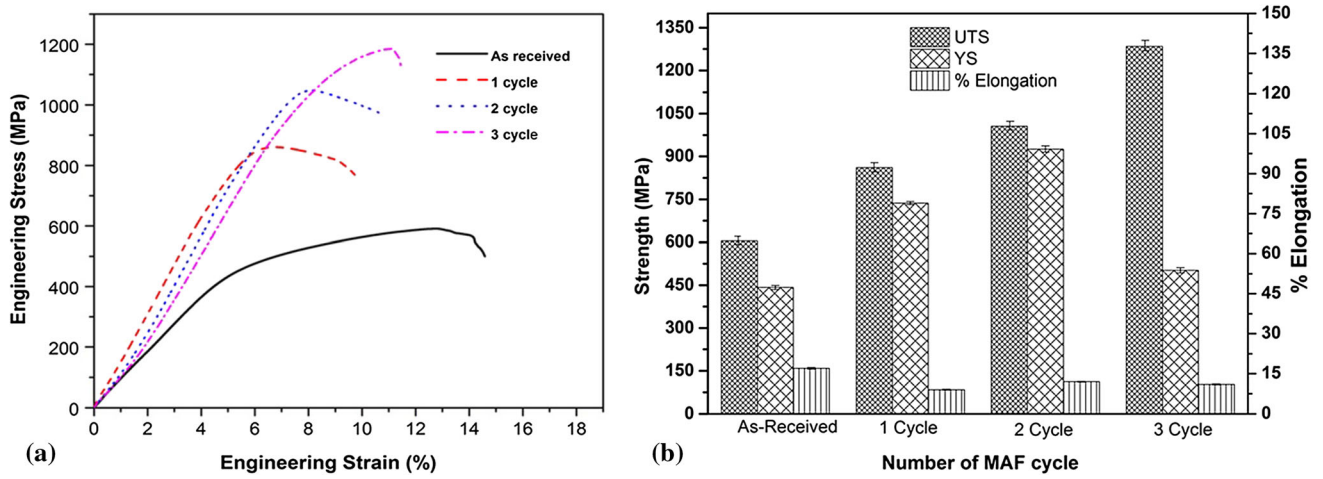


Fig. 9 (a) Stress–strain graph and (b) bar chart of mechanical properties of MAF-processed samples

Table 1 Mechanical properties of as-received and MAF-processed samples

Sample no.	UTS, MPa	YS, MPa	Elongation, %	Hardness, HV	Average grain size, $\mu\text{m}$
As-received	605 $\pm$ 6	442 $\pm$ 7	17 $\pm$ 0.48	252 $\pm$ 12	70 $\pm$ 8
One cycle	861 $\pm$ 8	737 $\pm$ 9	10 $\pm$ 0.2	358 $\pm$ 8	5 $\pm$ 2
Two cycles	1006 $\pm$ 12	926 $\pm$ 7	11 $\pm$ 0.3	392 $\pm$ 10	0.8
Three cycles	1284 $\pm$ 9	1007 $\pm$ 8	12 $\pm$ 0.25	428 $\pm$ 10	0.2

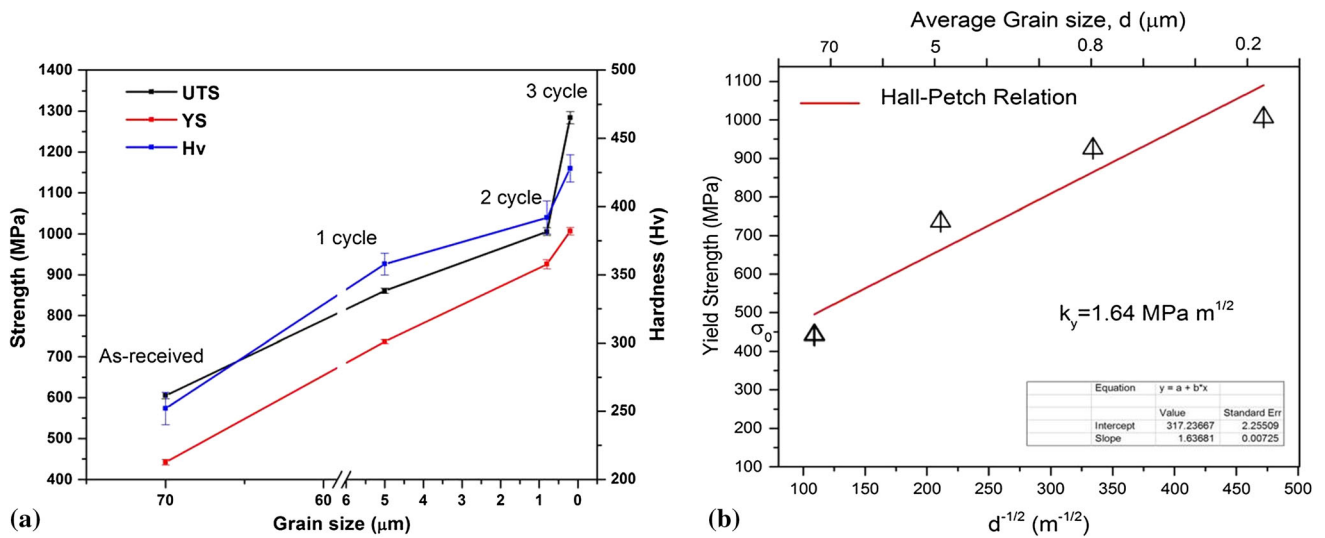
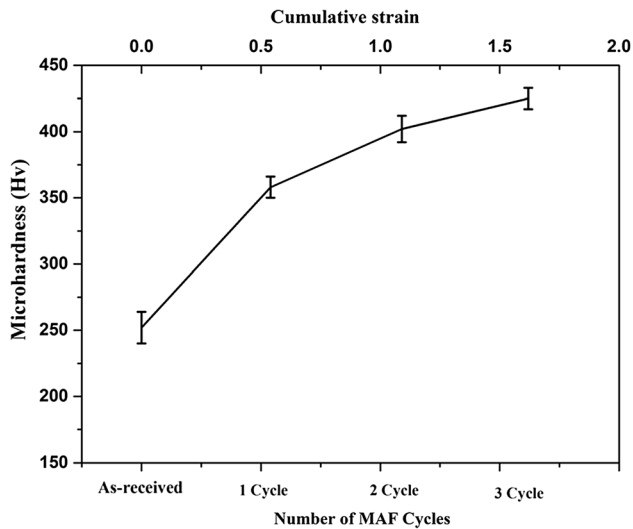


Fig. 10 (a) Relationship between mechanical properties (UTS, YS, and hardness) and average grain size and (b) yield strength v/s inverse square of grains (Hall–Petch relationship)



is observed that the dimple size increases to 8 and 14  $\mu\text{m}$ , respectively, after two and three cycles of MAF. Increase in dimple size after two cycles is because of the increase in the ductility of the material. This shows that dimple size is directly related to ductility of material. Reduction in dimple size in MAF-processed samples is due to work hardening and grain refinement.



**Fig. 11** Vickers micro-hardness of sample processed by different MAF cycles

### 3.6 Corrosion Studies

**3.6.1 Potentiodynamic Polarization and EIS.** Figure 13 shows potentiodynamic plot that was analyzed by Tafel fitting EC-lab version 10.37 and plotted for as-received and MAF-processed samples. Corrosion kinetics parameters like  $I_{\text{corr}}$  (corrosion current density),  $E_{\text{corr}}$  (corrosion potential), and corrosion rate (mm/y) were extracted and are tabulated in

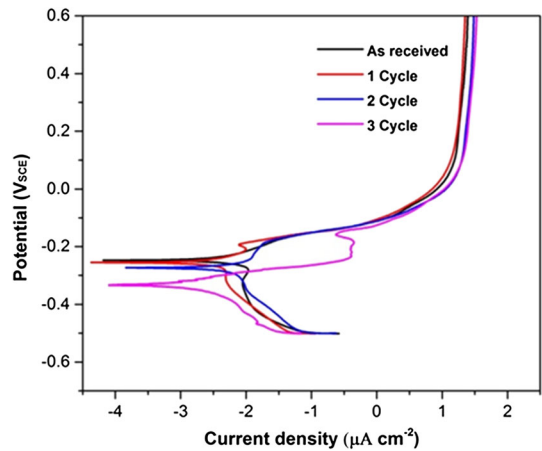


**Fig. 13** Potentiodynamic polarization of 4.5%Ti as-received and MAF-processed samples

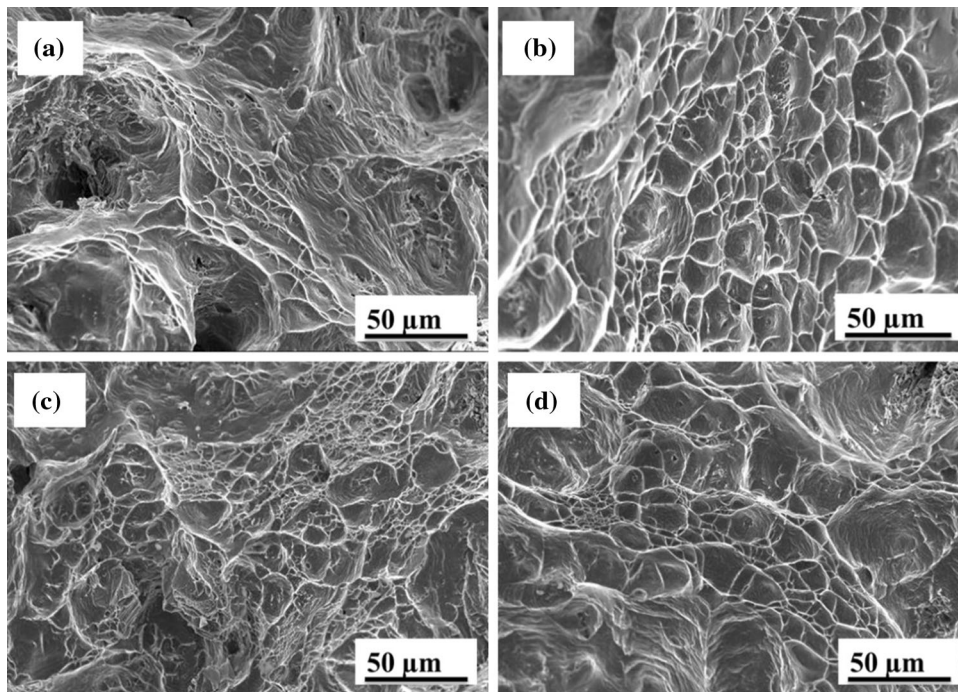


**Fig. 12** SEM micrograph of fracture surface after tensile test for samples processed by different MAF cycles: (a) as-received, (b) one cycle, (c) two cycles, and (d) three cycles

**Table 2 Corrosion properties of Cu-4.5%Ti of as-received and MAF-processed samples**

Sample condition	$E_{\text{corr}}$ V <sub>SCE</sub>	$i_{\text{corr}}$ $\mu\text{A}/\text{cm}^2$	Corrosion rate, mm/y
As-received	- 251.39	5.38	0.125
One cycle	- 234.0	4.24	0.098
Two cycles	- 246.88	3.52	0.072
Three cycles	- 251.88	2.82	0.055

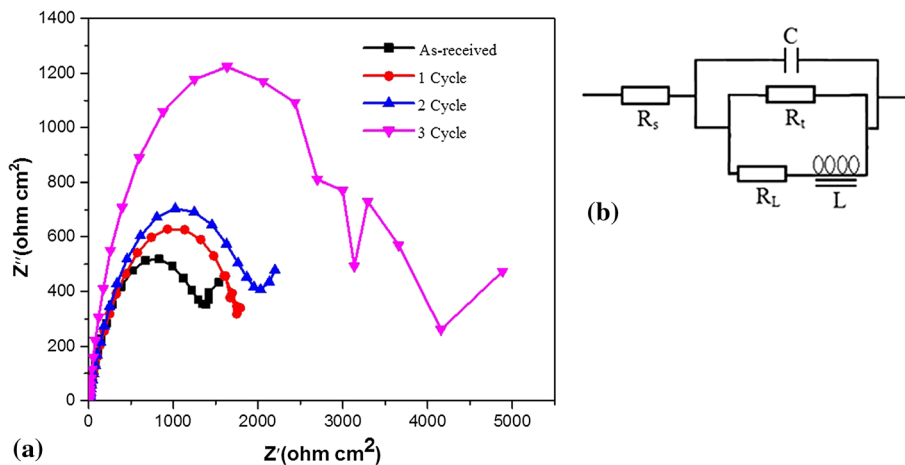
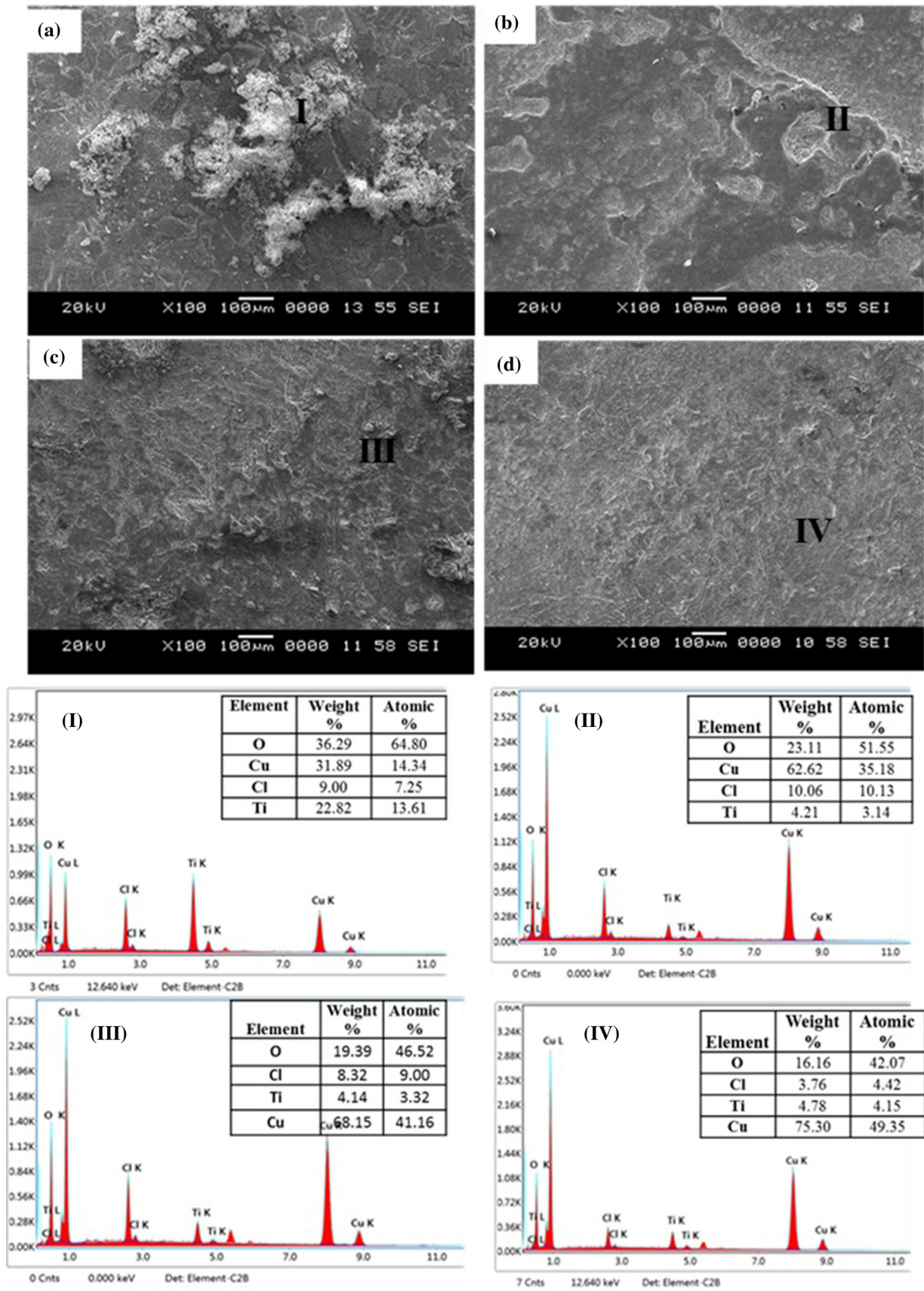
**Fig. 14** (a) Nyquist plots of as-received and MAF-processed samples and (b) equivalent circuit (Randles circuit) for analyzing of the EIS characteristics

Table 2. Low current density was observed for as-received sample compared to processed samples. As the number of MAF cycles increases,  $E_{\text{corr}}$  tends to shift toward the negative value.  $I_{\text{corr}}$  reduced with the increase in MAF cycles. Corrosion rate of Cu-4.5%Ti was found to be very high (0.093 mm/y) as compared to one cycle (0.064 mm/y), two cycles (0.054 mm/y), and three cycles (0.024 mm/y) of MAF-processed samples. Corrosion resistance of three cycles of MAF-processed samples was 3.87 times high as compared to that of as-received samples. Improvements in corrosion resistance were because of grain refinement where more grain boundaries acted as a corrosion barrier (Ref 42).

EIS plot was obtained for both as-received and MAF-processed conditions, and Fig. 14 shows Nyquist plot and equivalent Randles circuit of EIS data. A semicircle radius is associated with the metal dissolution in EIS. A semicircle diameter is concerned with the charge transfer resistance ( $R_t$ ), which is proportional to the corrosion resistance. The protective film formation of sample is represented by first semicircle that is called capacitance arc, and the tail region of semicircle is called inductive loop that is damaged or degraded protective layer. Diameter of the semicircles of capacitive arc is directly associated with the corrosion resistance. Figure 14(a) shows that diameter of capacitive arc is small as compared to that of

MAF-processed samples. Diameter of capacitive arc is increased with MAF pass which implies increased corrosion resistance. Reason for improved corrosion resistance of deformed sample is because of increased density of grain boundaries (Ref 43). Figure 14(b) represents the equivalent Randles circuit of EIS, and it consists of  $R_t$ ,  $R_L$ ,  $R_s$ ,  $C$ , and  $L$ .  $R_s$ ,  $R_t$ , and  $R_L$  denote electrolyte resistance, charge transfer resistance, and resistance of intermediate product, respectively. Constant phase element (CPE) shows the capacitive behavior of protective layer, and inductance is represented by  $L$ .

**3.6.2 Corrosion Surface Morphology.** SEM images of Cu-4.5%Ti sample after removing corrosion product from the surface are shown in Fig. 15. Intergranular and pitting corrosion was observed, because of susceptibility of copper to intergranular corrosion in chlorine solution. Pitting corrosion occurred because of micro-galvanic coupling between Cu and Ti. This figure also shows EDS analysis on the corroded surface. As-received sample produced oxide layer of 36.29 wt.%. With the increase in number of MAF cycles, oxide formation on sample surface reduced, because of increased grain boundaries which act as a corrosion barrier and increased the corrosion resistance. Figure 16 shows the XRD pattern of corroded sample processed by MAF for three cycles. CuCl and



**Fig. 15** SEM micrographs and EDS analysis of corrosion surface of (a) as-received and MAF-processed, (b) one cycle, (c) two cycles, and (d) three cycles of samples

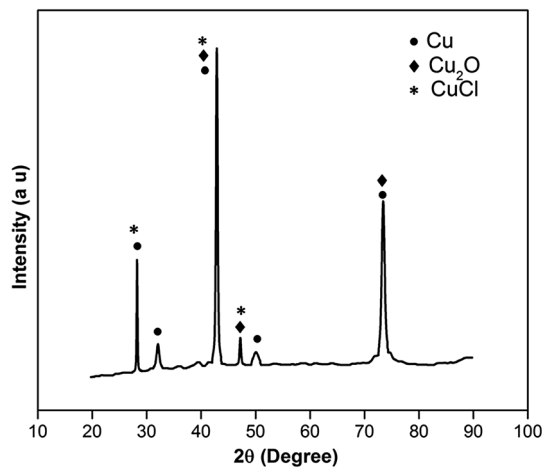


**Fig. 16** XRD analysis of corrosion product of three cycles of MAF-processed sample

Cu<sub>2</sub>O are the corrosion products observed in the XRD and act as protective passivation layer, which reduces the corrosion attack on the sample.

#### 4. Conclusions

MAF was used successfully to process Cu-4.5%Ti alloy up to three cycles for a cumulative strain of 1.64 at cryogenic temperature. Microstructure, mechanical, and corrosion properties were investigated. The following conclusions are derived from the current study.

1. After three cycles of MAF, grain size reduced from 70 μm to ~ 200 nm (as observed from TEM). Grain refinement is because of the formation of micro-shear bands. EBSD results show the transformation from HAGBs to LAGBs.
2. YS, UTS, and % elongation to failure increased with the increase in MAF cycles. Maximum UTS of 1284 MPa and YS 1007 MPa with 11% elongation were achieved after three cycles of MAF processing at cryogenic condition. Grain boundary strengthening is the mechanism behind the increase in strength.
3. Micro-hardness increased from 225 to 428 HV for three cycles of MAF-processed sample. Driving mechanisms of increased hardness are strain hardening and grain refinement.
4. Fracture surface revealed that dimple size decreases for the first cycle due to the decrease in ductility. After two cycles of MAF, a slight increase in dimples size was observed, because of the increase in ductility. After three cycles, surface looks to be of ductile-brittle kind of fracture.
5. Potentiodynamic polarization results show that corrosion resistance increases after MAF due to grain refinement. Corrosion surface morphology shows intergranular and

pitting corrosion, and EDS analysis shows formation of oxide layers on the corroded surface.

#### References

1. R.Z. Valiev, R.K. Islamgaliev, and I.V. Alexandrov, Bulk Nanostructured Materials from Severe Plastic Deformation, *Prog. Mater. Sci.*, 2000, **45**(2), p 103–189
2. R.Z. Valiev, Developing SPD Methods for Processing Bulk Nanostructured Materials with Enhanced Properties, *Met. Mater. Int.*, 2001, **7**(5), p 413–420
3. R. Valiev, Nanostructuring of Metals by Severe Plastic Deformation for Advanced Properties, *Nat. Mater.*, 2004, **3**(8), p 511
4. W. Chen, D. Ferguson, and H. Ferguson, Severe Plastic Deformation Techniques, *Acta Metall. Sin. (English Letters)*, 2009, **13**(1), p 242–253
5. Y. Estrin and A. Vinogradov, Extreme Grain Refinement by Severe Plastic Deformation: A Wealth of Challenging Science, *Acta Mater.*, 2013, **61**(3), p 782–817
6. K.R. Gopi, H.S. Nayaka, and S. Sahu, Investigation of Microstructure and Mechanical Properties of ECAP-Processed AM Series Magnesium Alloy, *J. Mater. Eng. Perform.*, 2016, **25**(9), p 3737–3745
7. K.R. Gopi, H.S. Nayaka, and S. Sahu, Microstructural Evolution and Strengthening of AM90 Magnesium Alloy Processed by ECAP, *Arab. J. Sci. Eng.*, 2017, **42**(11), p 4635–4647
8. K.R. Gopi, H.S. Nayaka, and S. Sahu, Wear Properties of ECAP-Processed AM80 Magnesium Alloy, *J. Mater. Eng. Perform.*, 2017, **26**(7), p 3399–3409
9. G. Anne, M.R. Ramesh, H.S. Nayaka, S.B. Arya, and S. Sahu, Development and Characteristics of Accumulative Roll Bonded Mg-Zn/Ce/Al Hybrid Composite, *J. Alloys Compd.*, 2017, **724**, p 146–154
10. G. Anne, M.R. Ramesh, H.S. Nayaka, S.B. Arya, and S. Sahu, Development and Properties Evaluation of Mg–6% Zn/Al Multilayered Composites Processed by Accumulative Roll Bonding, *J. Mater. Res.*, 2017, **32**(12), p 2249–2257
11. G. Anne, M.R. Ramesh, H.S. Nayaka, S.B. Arya, and S. Sahu, Microstructure Evolution and Mechanical and Corrosion Behavior of Accumulative Roll Bonded Mg-2%Zn/Al-7075 Multilayered Composite, *J. Mater. Eng. Perform.*, 2017, **26**(4), p 1726–1734
12. Q. Chen, D. Shu, C. Hu, Z. Zhao, and B. Yuan, Grain Refinement in an As-Cast AZ61 Magnesium Alloy Processed by Multi-axial Forging Under the Multitemperature Processing Procedure, *Mater. Sci. Eng. A*, 2012, **541**, p 98–104
13. P.N. Rao, D. Singh, and R. Jayaganthan, Mechanical Properties and Microstructural Evolution of Al 6061 Alloy Processed by Multidirectional Forging at Liquid Nitrogen Temperature, *Mater. Des.*, 2014, **56**, p 97–104
14. R. Gupta, S. Sivastava, N.K. Kumar, and S.K. Panthi, High Leaded tin Bronze Processing During Multi-directional Forging: Effect on Microstructure and Mechanical Properties, *Mater. Sci. Eng. A*, 2016, **654**, p 282–291
15. J. Huang, Y.T. Zhu, D.J. Alexander, X. Liao, T.C. Lowe, and R.J. Asaro, Development of Repetitive Corrugation and Straightening, *Mater. Sci. Eng. A*, 2004, **371**(1–2), p 35–39
16. B.R. Sunil, Repetitive Corrugation and Straightening of Sheet Metals, *Mater. Manuf. Process.*, 2015, **30**(10), p 1262–1271
17. Z. Horita and T.G. Langdon, Microstructures and Microhardness of an Aluminum Alloy and Pure Copper After Processing by High-Pressure Torsion, *Mater. Sci. Eng. A*, 2005, **410**, p 422–425
18. Y. Ivanisenko, R. Kulagin, V. Fedorov, A. Mazilkin, T. Scherer, B. Baretzky, and H. Hahn, High Pressure Torsion Extrusion as a New Severe Plastic Deformation Process, *Mater. Sci. Eng. A*, 2016, **664**, p 247–256
19. R. Kocich, L. Kunčická, and A. Macháčková, Twist Channel Multi-Angular Pressing (TCMAP) as a Method for Increasing the Efficiency of SPD, *IOP Conf. Ser. Mater. Sci. Eng.*, 2014, **63**(1), p 012006

20. R. Kocich, L. Kunčická, P. Král, and A. Macháčková, Sub-structure and Mechanical Properties of Twist Channel Angular Pressed Aluminium, *Mater. Charact.*, 2016, **119**, p 75–83
21. S. Swaminathan, M. Ravi Shankar, B.C. Rao, W.D. Compton, S. Chandrasekar, A.H. King, and K.P. Trumble, Severe Plastic Deformation (SPD) and Nanostructured Materials by Machining, *J. Mater. Sci.*, 2007, **42**(5), p 1529–1541
22. P.C. Yadav, S. Sahu, A. Subramaniam, and S. Shekhar, Effect of Heat-Treatment on Microstructural Evolution and Mechanical Behaviour of Severely Deformed Inconel 718, *Mater. Sci. Eng. A*, 2018, **715**, p 295–306
23. H. Miura, T. Maruoka, X. Yang, and J.J. Jonas, Microstructure and Mechanical Properties of Multi-directionally Forged Mg–Al–Zn Alloy, *Scr. Mater.*, 2012, **66**(1), p 49–51
24. A. Joshi, N. Kumar, K.K. Yogesha, R. Jayaganthan, and S.K. Nath, Mechanical Properties and Microstructural Evolution in Al 2014 Alloy Processed Through Multidirectional Cryoforging, *J. Mater. Eng. Perform.*, 2016, **25**(7), p 3031–3045
25. X.Y. Yang, Z.Y. Sun, J. Xing, H. Miura, and T. Sakai, Grain Size and Texture Changes of Magnesium Alloy AZ31 During Multi-directional Forging, *Trans. Nonferr. Met. Soc. China*, 2008, **18**, p s200–s204
26. A.K. Padap, G.P. Chaudhari, S.K. Nath, and V. Pancholi, Ultrafine-Grained Steel Fabricated Using Warm Multiaxial Forging: Microstructure and Mechanical Properties, *Mater. Sci. Eng.*, 2009, **527**(1–2), p 110–117
27. S.M. Dasharath and S. Mula, Mechanical Properties and Fracture Mechanisms of Ultrafine Grained Cu-9.6% Zn Alloy Processed by Multiaxial Cryoforging, *Mater. Sci. Eng. A*, 2016, **675**, p 403–414
28. W.E.I. Huan, L.F. Hou, Y.C. Cui, and Y.H. Wei, Effect of Ti Content on Corrosion Behavior of Cu-Ti Alloys in 3.5% NaCl Solution, *Trans. Nonferr. Met. Soc. China*, 2018, **28**(4), p 669–675
29. H. Wei, Y.H. Wei, L.F. Hou, and N. Dang, Correlation of Ageing Precipitates with the Corrosion Behaviour of Cu-4 wt.% Ti Alloys in 3.5 wt.% NaCl Solution, *Corros. Sci.*, 2016, **111**, p 382–390
30. D. Wang, B. Xiang, Y. Liang, S. Song, and C. Liu, Corrosion Control of Copper in 3.5 wt.% NaCl Solution by Domperidone: Experimental and Theoretical Study, *Corros. Sci.*, 2014, **85**, p 77–86
31. A. Szkliniarz, L. Blacha, W. Szkliniarz, and J. Łabaj, Characteristics of Plasticity of Hot Deformed Cu-Ti Alloys, *Arch. Metall. Mater.*, 2014, **59**(4), p 1307–1312
32. C. Kobayashi, T. Sakai, A. Belyako, and H. Miura, Ultrafine Grain Development in Copper During Multidirectional Forging at 195 K, *Philos. Mag. Lett.*, 2007, **87**(10), p 751–766
33. S. Sahu, P.C. Yadav, and S. Shekhar, Use of Hot Rolling for Generating Low Deviation Twins and a Disconnected Random Boundary Network in Inconel 600 Alloy, *Metall. Mater. Trans. A*, 2017, **49**(2), p 628–643
34. S. Sahu, N.K. Sharma, S.K. Patel, K. Mondal, and S. Shekhar, The Effect of Grain Boundary Structure on Sensitization Behavior in a Nickel-Based Superalloy, *J. Mater. Sci.*, 2019, **54**, p 1797–1818
35. P.C. Yadav, A. Sinhal, S. Sahu, A. Roy, and S. Shekhar, Microstructural Inhomogeneity in Constrained Groove Pressed Cu-Zn Alloy Sheet, *J. Mater. Eng. Perform.*, 2016, **25**(7), p 2604–2614
36. K.S.V.B.R. Krishna, M. Ashfaq, V. Varun, K. Sivaprasad, K. Venkateswarlu, and S.S.R. Akella, On Plastic Deformation Behavior of Cryorolled AA8090 Alloy, *Trans. Indian Inst. Met.*, 2017, **70**(6), p 1463–1475
37. M. Dao, L. Lu, Y.F. Shen, and S. Suresh, Strength, Strain-Rate Sensitivity and Ductility of Copper with Nanoscale Twins, *Acta Mater.*, 2006, **54**(20), p 5421–5432
38. T.G. Nieh and J. Wadsworth, Hall-Petch Relation in Nanocrystalline Solids, *Scr. Metall. Mater.*, 1991, **25**, p 955
39. P.E.N.G. Luo, D.T. McDonald, W. Xu, S. Palanisamy, M.S. Dargusch, and K.E.N.O.N.G. Xia, A Modified Hall-Petch Relationship in Ultrafine-Grained Titanium Recycled from Chips by Equal Channel Angular Pressing, *Scr. Mater.*, 2012, **66**(10), p 785–788
40. P. Luo, Q. Hu, and X. Wu, Quantitatively Analyzing Strength Contribution vs Grain Boundary Scale Relation in Pure Titanium Subjected to Severe Plastic Deformation, *Meta. Mater. Trans. A*, 2016, **47**(5), p 1922–1928
41. P. Luo, Analysis of Microstructure and Its Effect on Yield Strength of Pure Alpha-Titanium Consolidated by Equal Channel Angular Pressing, *Mater. Trans.*, 2018, **59**(7), p 1161–1165
42. J. Jiang, M.A. Aibin, N. Saito, S.H.E.N. Zhixin, S.O.N.G. Dan, L.U. Fumin, Y. Nishida, Y.A.N.G. Donghui, and L.I.N. Pinghua, Improving Corrosion Resistance of RE-Containing Magnesium Alloy ZE41A Through ECAP, *J. Rare Earths*, 2009, **27**(5), p 848–852
43. K.D. Ralston and N. Birbilis, Effect of Grain Size on Corrosion: A Review, *Corrosion*, 2010, **66**(7), p 075005

**Publisher's Note** Springer Nature remains neutral with regard to jurisdictional claims in published maps and institutional affiliations.